NASA/TM–2013-217967

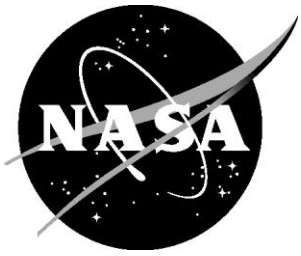

Buckling Analysis of a Honeycomb-Core Composite Cylinder with Initial Geometric Imperfections

Gene Cha
Texas A&M University, College Station, Texas

Marc R. Schultz
Langley Research Center, Hampton, Virginia

February 2013

NASA STI Program . . . in Profile

Since its founding, NASA has been dedicated to the advancement of aeronautics and space science. The NASA scientific and technical information (STI) program plays a key part in helping NASA maintain this important role.

The NASA STI program operates under the auspices of the Agency Chief Information Officer. It collects, organizes, provides for archiving, and disseminates NASA's STI. The NASA STI program provides access to the NASA Aeronautics and Space Database and its public interface, the NASA Technical Report Server, thus providing one of the largest collections of aeronautical and space science STI in the world. Results are published in both non-NASA channels and by NASA in the NASA STI Report Series, which includes the following report types:

- TECHNICAL PUBLICATION. Reports of completed research or a major significant phase of research that present the results of NASA Programs and include extensive data or theoretical analysis. Includes compilations of significant scientific and technical data and information deemed to be of continuing reference value. NASA counterpart of peer-reviewed formal professional papers, but having less stringent limitations on manuscript length and extent of graphic presentations.

- TECHNICAL MEMORANDUM. Scientific and technical findings that are preliminary or of specialized interest, e.g., quick release reports, working papers, and bibliographies that contain minimal annotation. Does not contain extensive analysis.

- CONTRACTOR REPORT. Scientific and technical findings by NASA-sponsored contractors and grantees.

- CONFERENCE PUBLICATION. Collected papers from scientific and technical conferences, symposia, seminars, or other meetings sponsored or co-sponsored by NASA.

- SPECIAL PUBLICATION. Scientific, technical, or historical information from NASA programs, projects, and missions, often concerned with subjects having substantial public interest.

- TECHNICAL TRANSLATION. English-language translations of foreign scientific and technical material pertinent to NASA's mission.

Specialized services also include organizing and publishing research results, distributing specialized research announcements and feeds, providing information desk and personal search support, and enabling data exchange services.

For more information about the NASA STI program, see the following:

- Access the NASA STI program home page at *http://www.sti.nasa.gov*

- E-mail your question to help@sti.nasa.gov

- Fax your question to the NASA STI Information Desk at 443-757-5803

- Phone the NASA STI Information Desk at 443-757-5802

- Write to:
  STI Information Desk
  NASA Center for AeroSpace Information
  7115 Standard Drive
  Hanover, MD 21076-1320

NASA/TM–2013-217967

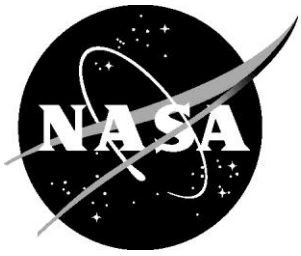

Buckling Analysis of a Honeycomb-Core Composite Cylinder with Initial Geometric Imperfections

Gene Cha
Texas A&M University, College Station, Texas

Marc R. Schultz
Langley Research Center, Hampton, Virginia

National Aeronautics and
Space Administration

Langley Research Center
Hampton, Virginia 23681-2199

February 2013

Acknowledgments

This report documents work that was begun while the first author was a Langley Aerospace Research Student Scholar (LARSS) working in the Structural Mechanics and Concepts Branch at NASA Langley Research Center. The work is part of the NASA Engineering and Safety Center (NESC) Shell Buckling Knockdown Factor Project, NESC assessment number 07-010-E. The composite cylinder analyzed in this work was manufactured and provided by Northrop Grumman Corporation. The authors appreciate the advice of Drs. Mark W. Hilburger and Waddy T. Haynie of the Structural Mechanics and Concepts Branch at NASA Langley Research Center.

Available from:

NASA Center for AeroSpace Information
7115 Standard Drive
Hanover, MD 21076-1320
443-757-5802

Abstract

Thin-walled cylindrical shell structures often have buckling as the critical failure mode, and the buckling of such structures can be very sensitive to small geometric imperfections. The buckling analyses of an 8-ft-diameter, 10-ft-long honeycomb-core composite cylinder loaded in pure axial compression is discussed in this document. Two loading configurations are considered–configuration 1 uses simple end conditions, and configuration 2 includes additional structure that may more closely approximate experimental loading conditions. Linear eigenvalue buckling analyses and nonlinear analyses with and without initial geometric imperfections were performed on both configurations. The initial imperfections were introduced in the shell by applying a radial load at the midlength of the cylinder to form a single inward dimple. The critical bifurcation buckling loads are predicted to be 924,190 lb and 924,020 lb for configurations 1 and 2, respectively. Nonlinear critical buckling loads of 918,750 lb and 954,900 lb were predicted for geometrically perfect configurations 1 and 2, respectively. Lower-bound critical buckling loads for configurations 1 and 2 with radial perturbations were found to be 33% and 36% lower, respectively, than the unperturbed critical loads. The inclusion of the load introduction cylinders in configuration 2 increased the maximum bending-boundary-layer rotation up to 11%.

THIS PAGE INTENTIONALLY LEFT BLANK

Nomenclature

E	Isotropic elastic modulus
E_1, E_2, E_3	Orthotropic elastic moduli in the material 1, 2, and 3 directions, respectively
E_y, E_z	Circumferential and axial effective engineering elastic modulus of the composite facesheets, respectively
G_{12}, G_{13}, G_{23}	Orthotropic shear moduli in the material 12, 13, and 23 directions, respectively
G_{xzc}	Transverse shear modulus of the honeycomb core in the *xz* plane
hc	Honeycomb core thickness
P	Applied compressive load
P_{bif}	Lowest linear buckling load
P_{cr}	Nonlinear critical buckling load
Q	Applied radial load
R	Cylinder midsurface radius
t_f	Composite facesheet thickness
U_x, U_y, U_z	Displacement in the outward normal, circumferential, and axial direction, respectively
UR_x, UR_y, UR_z	Rotations about the outward normal, circumferential, and axial coordinates, respectively
v	Isotropic Poisson's ratio
v_{12}, v_{13}, v_{23}	Orthotropic Poisson's ratios in the material 12, 13, and 23 directions, respectively
v_{yz}, v_{zy}	Effective engineering Poisson's ratio in the *yz* and *zy* planes
$(\sigma_{fz})_{bif}$	Average axial critical buckling stress in the facesheets

Subscripts

1, 2, 3	Material-direction coordinates in the fiber or ribbon direction, the in-plane transverse direction, and the thickness direction, respectively
x, y, z	Cylindrical midsurface coordinates in the outward normal, circumferential, and axial direction.

I. Introduction

The design of thin-walled cylindrical structures such as those in launch-vehicle barrel sections is often controlled by the buckling response. Additionally, the buckling response of such thin-walled cylinders is often sensitive to small geometric imperfections. To account for this imperfection sensitivity during the design process, so-called knockdown factors are used in design to reduce linear bifurcation-buckling buckling predictions to safe levels. The most used source of knockdown factors for cylindrical shells is NASA SP-8007 [1], which is based on empirical studies, was last updated in 1968, is considered overly conservative for many shell designs [2], and does not consider the design space of many modern launch-vehicle shells. NASA's Shell Buckling Knockdown Factor (SBKF) project is developing new analysis-based knockdown factors to update SP-8007 [3]. Several analysis methods can be used to predict lower-bound buckling loads for cylindrical shells under axial compression. Incorporating realistic manufacturing imperfection signatures in nonlinear buckling analyses is one approach for developing analysis-based knockdown factors [4]. However, these imperfection signatures are often not available during the design stage, before cylinders have been built. Therefore, other analysis approaches may be needed to simulate geometric imperfections. In Ref. [5], the effects of three other geometric imperfection types similar to those shown in Figure 1 were studied: eigenmode imperfections, radial perturbation loads at the midlength of the cylinder, and single stress-free dimple imperfections at the midlength of the cylinder. It was shown that the mode-shape imperfection has a significant effect on the buckling load and the effective axial stiffness. In contrast, it was shown that the radial perturbation and single dimple methods affect the buckling load without significantly affecting the effective axial stiffness. The study confirmed an earlier suggestion that the radial perturbation approach was a good method to develop improved, less conservative shell-buckling design loads [6]. The SBKF project primarily uses the radial perturbation method for determining lower-bound buckling knockdown factors [7].

Fiber-reinforced composite materials can have advantages that lead to their use for certain launch-vehicle structures. These advantages can include high specific strength and stiffness, and good environmental and fatigue resistance when compared with metals. The design of thin-walled cylindrical structures such as those in launch-vehicle barrel sections is often controlled by the buckling response. Therefore, sandwich composites, which consist of a lightweight core and thin high strength and stiffness facesheets, are often chosen for such structures because the specific bending stiffness and buckling resistance can be increased simply by increasing the core thickness.

Aerospace-grade fiber-reinforced composite structures are generally cured and consolidated under heat and pressure in an autoclave. The pressure helps increase consolidation, reduce voids, and improve bonding between plies; the heat provides the energy for the curing process. The size of an autoclave limits the size of the products that can be produced in it, and many of the large space structures that are being designed or envisioned are larger than any existing autoclaves. Therefore, either larger autoclaves or alternative manufacturing methods are needed to produce unjointed structures. If appropriate quality can be obtained, out-of-autoclave composite manufacturing is an alternative to autoclave curing that could reduce manufacturing cost.

This report considers buckling predictions for an out-of-autoclave honeycomb-core sandwich composite cylinder that is intended to be tested as part of the SBKF project. Linear-eigenvalue

and geometrically nonlinear static finite-element analyses (FEA) with different values of radial perturbation load were conducted. Additionally, closed-form eigenvalue analyses were conducted as a check on the FEA. The test-article design and modeling details are given in Section II. The analysis results are presented and discussed in Section III, and concluding remarks are made in Section IV.

II. Problem Description

A. Test-Article Design

The test article considered in this report was manufactured by the Northrop Grumman Corporation, and is a unitized out-of-autoclave honeycomb-core sandwich composite cylinder (Figure 2 and Figure 3) that has an outside diameter of 95.29 in. and a length of 120 in. The core is ¼-in.-thick 4.5 lb/ft^3 Kevlar/phenolic honeycomb with 1/8-in. cells. The facesheets are seven-ply IM7/MTM45 laminates with the stacking sequence of $[45/-45/0/90/0/-45/45]_T$ (where the "T" subscript denotes total layup), and the axial direction is the 0-degree direction. The plies are assumed to be 0.0052-in. thick.

Table 1 presents the material properties assumed for the analysis of the sandwich panel.

Twenty-inch-long pad-ups were secondarily bonded to both faces of each end to help reduce stress concentrations near the ends (Figure 4). The pad-ups are 6-ply IM7/MTM45 laminates consisting of only ±45° plies that step down in three ±45 pairs. Additionally, as shown in Figure 4 and Figure 5, 3.4 in. on either end will be potted, i.e., bonded, into metallic end rings that are constructed of 6061-T6 aluminum.

B. Finite-Element Models and Analysis Details

The study used the general-purpose finite-element code, Abaqus [8], and the models consisted of three-dimensional shell elements. The Abaqus S4 element, a four-noded doubly curved general-purpose shell element with finite membrane strains, was used exclusively in the considered finite-element analyses. The cylinder was modeled as a single shell with honeycomb core modeled as an additional ply; this approach is typically adequate to model thin-shelled honeycomb-core sandwich structures.

Two configurations were considered in the modeling—*configuration 1* included only the barrel with the end rings approximated through the use of boundary conditions, and *configuration 2* more closely approximated the loading condition in a likely to be used test rig by including steel load-introduction cylinders at either end of the test article. The size and design of the end rings and the load-introduction cylinders is depicted in Figure 5. The load-introduction cylinders were made of A36 carbon steel (Table 1), and it should be noted that the midsurfaces of the load-introduction cylinders had a 1.25-in. larger diameter than the test article.

In configuration 1, the loading and boundary conditions were applied directly to the cylinder as shown in Figure 6. To simulate the potting, the nodes in the potted region were free in the axial direction and fixed in all others. One end of the cylinder was fixed in the axial direction, and the compressive load was applied to the other end. The axial displacements of all the loading-end nodes were tied a central node with a rigid body link to enforce a uniform displacement

condition, and a compression load was applied to that central node. This end condition is similar to applying compression in a load frame with rigid platens. To determine the mesh that would be used in the analyses, a mesh convergence study that compared critical buckling eigenvalues was performed with uniform meshes that had elements approximately 5-in., 2-in., 1-in., and 0.5-in. square. The critical buckling eigenvalue predicted with the 5-in. mesh was 11% higher than that predicted with the 2-in. mesh. Additionally, the critical eigenvalue predicted with the 2-in. mesh was 1.8% higher than that predicted with the 1-in. mesh; and the critical eigenvalue predicted with the 1-in. mesh was only 0.4% higher than that predicted with 0.5-in. mesh. Because the 0.5-in. mesh took a considerable time to run, the 1-in. mesh was used for subsequent analyses. This 1-in. mesh had 121 elements in axial direction and 300 elements in the circumferential direction on the cylinder.

The model for configuration 2 consisted of a three-part assembly—the test-article cylinder with the attached end rings, and the two load-introduction cylinders. All three parts were modeled with shell elements and included an attachment-flange detail, which was modeled as a ring of shell elements. The assembled state is shown in Figure 7. One load-introduction-cylinder end flange was constrained in all degrees of freedom, and the other load-introduction-cylinder flange was constrained in all degrees of freedom except the axial direction. In a manner similar to configuration 1, the load was applied at a central node that was tied to the end nodes with rigid links. As shown in Figure 5, the midsurface diameter of the load-introduction fixture was 1.25-in. larger than the midsurface diameter of the test-article cylinder. This misalignment was important to include in the models because of the potential for rotation at the interface between specimen and fixtures. To determine the mesh that would be used in the configuration 2 analyses, a mesh convergence study that compared critical buckling eigenvalues was performed with uniform meshes in the specimen that had elements approximately 5-in., 2-in., 1-in., and 0.5-in. square. This mesh convergence case study showed similar behavior to that seen for configuration 1, and similarly the 1-in mesh was chosen for further analyses. The flange part of the specimen was considered to be 1.5-in. thick 6061-T6 aluminum (Table 1), and the last 3.4-in. of both ends of the specimen have outer 0.5-in. and inner 0.4-in.-thick 6061-T6 aluminum layers with composite sandwich panel in the center to simulate the potted region as depicted in left picture of Figure 5. A separate mesh convergence study also showed that the eigenvalues were almost the same as the load-introduction-cylinder mesh was varied from 1 to 5 in. with the 1-in. specimen mesh. Therefore, a 1-in. mesh was also chosen for the load-introduction cylinders.

Two analysis types were performed for each configuration—linear eigenvalue buckling analyses, and geometrically nonlinear static analyses. For the eigenvalue analyses, a 100 lb compression load was applied, the Lanczos eigensolver was used, and the first five eigenmodes were calculated. The linear analysis result can confirm if the nonlinear FEA models are valid. For the nonlinear analyses, radial perturbation loads ranging from 0 to 1,000 lb were applied to the mid-length of the test article, as shown in Figure 6 and Figure 7. With the radial load applied, the compression load was increased until either negative roots in the stiffness matrix (which are reported as “negative eignevalues” by Abaqus) were encountered, or until a converged solution could not be found. In either case, the analysis was restarted with a smaller increment size from the last converged solution without reported negative eigenvalues. This restarting procedure was repeated until the increment size is less than 1% from previous converged increment. The maximum load at the last increment is considered as the critical buckling load.

III. Predictions of Cylinder Response

This section presents the analysis results of the linear buckling and geometrically nonlinear static analyses. In the linear eigenvalue buckling study, the geometrically perfect cylinder was examined through FEA and closed-form analytical calculations. The nonlinear analyses were used to investigate the buckling behavior of the cylinder under axial compression with radial perturbation loads ranging from 0 to 1,000 lb.

A. Linear Buckling Results

In this section, the linear buckling analysis results for configurations 1 and 2 using finite-element analysis, and a simplified configuration using closed-form equations are discussed.

Consider first the linear-buckling finite-element results. Table 2 presents buckling loads for the first five modes for both configurations. The critical bifurcation buckling load, P_{bif}, was predicted to be 924,190 lb and 924,020 lb for configurations 1 and 2, respectively, and the first five modes were all within 0.2% of the critical buckling load for both configurations. The configuration 1 critical buckling load was only 0.02% higher than that of configuration 2. It is seen in Figure 8 that the predicted critical buckling modes for configurations 1 and 2 were also very similar and exhibited an axisymmetric response.

The finite-element results were checked with the known closed-form solution developed by Reese and Bert [9], which is used to calculate the critical buckling stress for a cylindrical sandwich shell with simply supported edges and orthotropic faces under uniform axial compression. Effective engineering properties are used for the faces and core. The average critical buckling stress in the facesheets, $\left(\sigma_{fx}\right)_{bif}$, is calculated by Reese and Bert [9]:

$$\left(\sigma_{fz}\right)_{bif} = \frac{hc+t_f}{R}\left(\frac{E_y E_z}{1-\nu_{yz}\nu_{zy}}\right)^{\frac{1}{2}}\left\{1-\frac{hc\cdot t_f}{2(hc+t_f)R}\left(\frac{E_y E_z/{G_{xzc}}^2}{1-\nu_{yz}\nu_{zy}}\right)^{\frac{1}{2}}\right\} \tag{1}$$

where the subscripts y and z designate circumferential and axial directions, respectively, t_f is the facesheet thickness, the E's are elastic moduli, the ν's are Poisson's ratios, hc is the core thickness, G_{xzc} is the core transverse-shear modulus, and R is cylinder's midsurface radius. To compare with the critical buckling loads from the finite-element analyses, $\left(\sigma_{fx}\right)_{bif}$ needs to be converted to a buckling load. The critical load, P_{cr}, can be calculated by simply multiplying with composite facesheet's cross section area as

$$P_{bif} = \left(\sigma_{fz}\right)_{bif} \times 2R\pi \times 2t_f \tag{2}$$

For the current effort, the software package The Laminator [10], a composite layup calculator, was used to compute the effective engineering properties of the composite faces (Table 3). The calculated buckling load using this closed-form approach was 905,440 lb. Though the boundary conditions were different, this buckling load agreed well (approximately 2% lower) with the configuration 1 and 2 finite-element predictions of 924,190 lb and 924,020 lb, respectively.

B. Nonlinear Static Buckling Results

Results from geometrically nonlinear analyses of configuration 1 and 2 under compression loads, and compression loads with radial perturbation loads are discussed in this section.

Using the procedure discussed in Section IIB, buckling loads of 918,750 lb and 954,900 lb were obtained in the nonlinear analyses of configurations 1 and 2, respectively, under compression loads with no radial perturbation. The nonlinear buckling load for configuration 1 was 0.6% lower than its first linear eigenvalue buckling load and the nonlinear buckling load for configuration 2 was about 3.2% higher than its first linear eigenvalue buckling load. It is therefore seen that the configuration-1 and -2 end conditions had a greater effect in the nonlinear analyses than in the linear analyses. As seen in Figure 9, the load versus axial shortening responses for both configurations exhibited a linear prebuckling response, and for all values of radial perturbation load the configuration 1 and 2 critical loads were within 4%. The nonlinear buckling analyses showed 12 half-waves in the prebuckling deformations of both configurations 1 and 2 (Figure 10), as compared to the 11 half-waves that were seen in the first linear buckling mode of both configurations (Figure 8).

A radial perturbation load applied to the midlength of a thin-shell cylinder causes a geometric imperfection in the form of a single dimple and reduces the predicted buckling load of the cylinder. Figure 11 shows the normalized nonlinear critical buckling load, P_{cr}/P_{bif}, as a function of the applied radial load, Q. It is seen that the results for each configuration are similar and each exhibited a bilinear response. A similar type of bilinear response was seen in Refs. [5, 6]. It is seen that the higher-radial-load line has a slope close to zero, and the intersection of the two lines can be considered a practical lower-bound prediction [6]. The intersections of the two slopes are within 4.7% of each other: at 441 lb and a normalized critical load, P_{cr}/P_{bif}, of 0.67 for configuration 1, and at 451 lb and P_{cr}/P_{bif} of 0.64 for configuration 2.

The plots in Figure 12 show the critical buckling load versus end-shortening curves for different radial perturbation load values. For low radial perturbation loads, the curves are essentially linear up to the critical load. However, for radial perturbation loads greater than 700 lb, the curves are bilinear—initially the slope is similar to that of the low-radial-load curves, but at a point above 300 kips, the slope is reduced and continues essentially linearly until the critical load is reached. The change in slope is associated with stable local buckling that occurred at the point of application of the radial load. Figure 13 shows the radial displacement at the point of application of the radial load plotted as a function of the test-article axial shortening. It is seen that radial perturbation loads greater than 700 lb produced dramatic radial displacement changes that were associated with the local buckling event.

When compressive loads were applied, the test cylinder expanded due to Poisson effects, but the constrained boundaries restrained the expansion. This led to rotations near the boundaries. Additionally, as mentioned earlier, the load-introduction cylinder's diameter was 1.25-in. larger than the test article in configuration 2. Figure 14 shows the rotation about the circumferential coordinate (UR_y) for both configurations with no radial perturbation load. The configuration 2 diameter difference along with the compliance of the load introduction cylinder allows additional rotation (Figure 14b) when compared with configuration 1 (Figure 14a). Figure 15 presents the UR_y rotation as a function of the radial perturbation load. Similar to the behavior of the P_{cr}/P_{bif} ratio, the UR_y rotation near the fixtures exhibited a bilinear behavior with radial load. From these

figures, it is seen that the maximum amount of tangential rotation in configuration 2 was 11% higher than that in configuration 1 with no radial perturbation load. Therefore, care will need to be taken to include the load-introduction structure when planning experiments or performing pretest predictions.

IV. Concluding Remarks

Linear and nonlinear computational analyses were used to explore the buckling sensitivity of a compression-loaded 96-in.-diameter and 120-in.-long honeycomb-core sandwich composite cylinder that is representative of a potential test article. Two boundary and loading conditions were considered: configuration 1 approximated compressing the test article between two rigid plates, and configuration 2 more closely approximated an experimental loading condition by including steel load-introduction cylinders on the both ends of the test article and compressing the specimen between the steel cylinders. In configuration 2, the mid-surface diameter of the load-introduction cylinders was 1.25-in. larger than the mid-surface diameter of the test-article cylinder. It was found that the predicted nonlinear buckling load of the perfect cylinder was within 3% of the linear bifurcation buckling load for both configurations. The buckling sensitivity to geometric imperfections was explored by applying radial perturbation loads to the midlength of the test article. It was found that the application of these perturbation loads reduced the critical buckling load by up to 36%. The configuration 1 and 2 critical loads were within 4% for all radial perturbation loads. The compliance of the load introduction cylinders and the diameter misalignment in configuration 2 led to a rotation issue at the interface between specimen and fixtures. The predicted amount of tangential rotation near the fixtures was 11% higher for configuration 2 than for configuration 1 with no perturbation load.

References

1. Anonymous. "Buckling of Thin-Walled Circular Cylinders," *NASA Space Vehicle Design Criteria, NASA SP-8007*, 1965 (revised 1968).

2. Arbocz, J., and Starnes Jr, J. H. "Future Directions and Challenges in Shell Stability Analysis," *Thin-Walled Structures*, Vol. 40, No. 9, 2002, pp. 729-754.

3. Hilburger, M. W. "Developing the Next Generation Shell Buckling Design Factors and Technologies," *Proceedings of the 53rd AIAA/ASME/ASCE/AHS/ASC Structures, Structural Dynamics and Materials Conference*, AIAA paper no. 2012-1686, Honolulu, HI, April 2012.

4. Hilburger, M. W., Nemeth, M. P., and Starnes, J. H. "Shell Buckling Design Criteria Based on Manufacturing Imperfection Signatures," *AIAA Journal*, Vol. 44, No. 3, 2006, pp. 654-663.

5. Haynie, W. T., and Hilburger, M. W. "Comparison of Methods to Predict Lower Bound Buckling Loads of Cylinders Under Axial Compression," *Proceedings of the 51st AIAA/ASME/ASCE/AHS/ASC Structures, Structural Dynamics, and Materials Conference*, AIAA paper no. 2010-2532, Orlando, FL, April 2010.

6. Hühne, C., Rolfes, R., Breitbach, E., and Teßmer, J. "Robust Design of Composite Cylindrical Shells under Axial Compression—Simulation and Validation," *Thin-Walled Structures*, Vol. 46, No. 7, 2008, pp. 947-962.

7. Haynie, W. T., and Hilburger, M. W., Private Conversations, May 2012.

8. Abaqus, Software Package, Ver. 6.12. Dassault Systèmes, Waltham, MA, 2012.

9. Reese, C. D., and Bert, C. W. "Simplified Design Equations for Buckling of Axially Compressed Sandwich Cylinders with Orthotropic Facings and Core," *Journal of Aircraft*, Vol. 6, No. 6, 1969, pp. 515-519.

10. The Laminator, Software Package, Ver. 3.7, Mike Lindell, 2011, www.thelaminator.net.

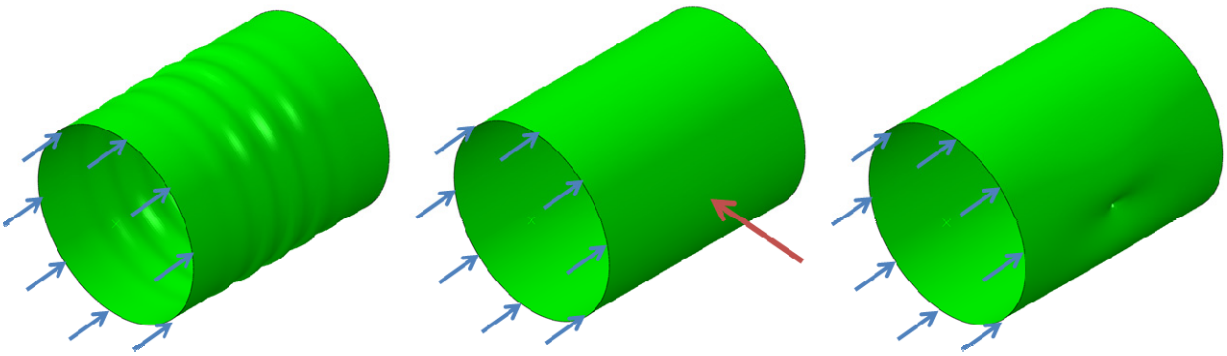

(a) Mode-shape imperfection (b) Radial perturbation (c) Stress-free single dimple

Figure 1. Three ways to introduce geometrical imperfections: (a) mode-shape imperfection, (b) radial perturbation load, and (c) stress-free single dimple.

Figure 2. The physical test article analyzed herein.

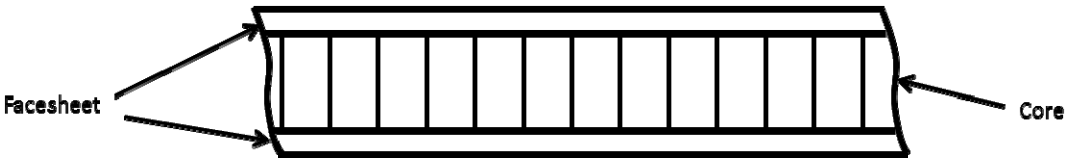

Figure 3. Typical cross-sectional view of a sandwich composite.

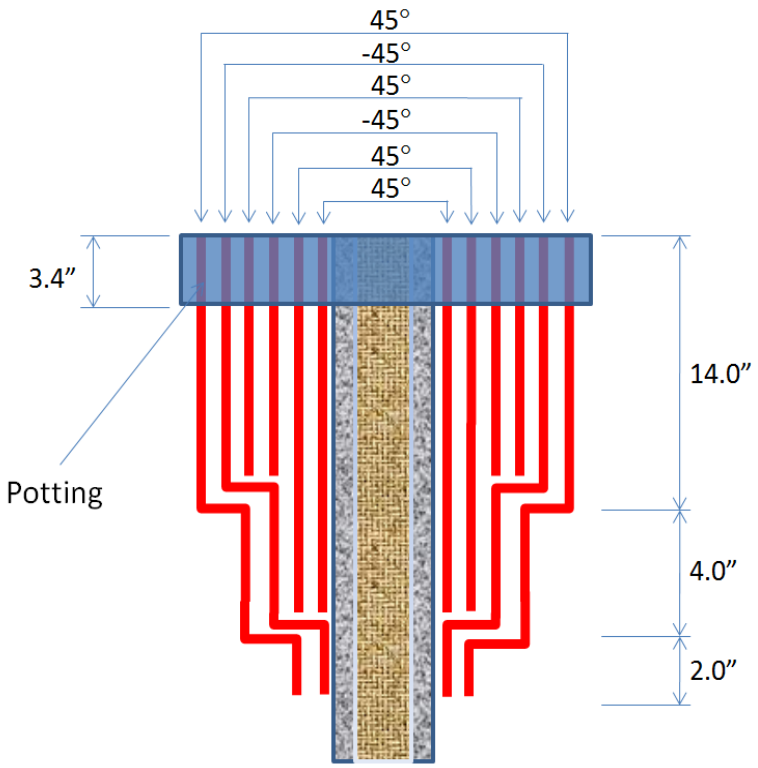

Figure 4. Cross-sectional schematic of the pad-up region of the test article.

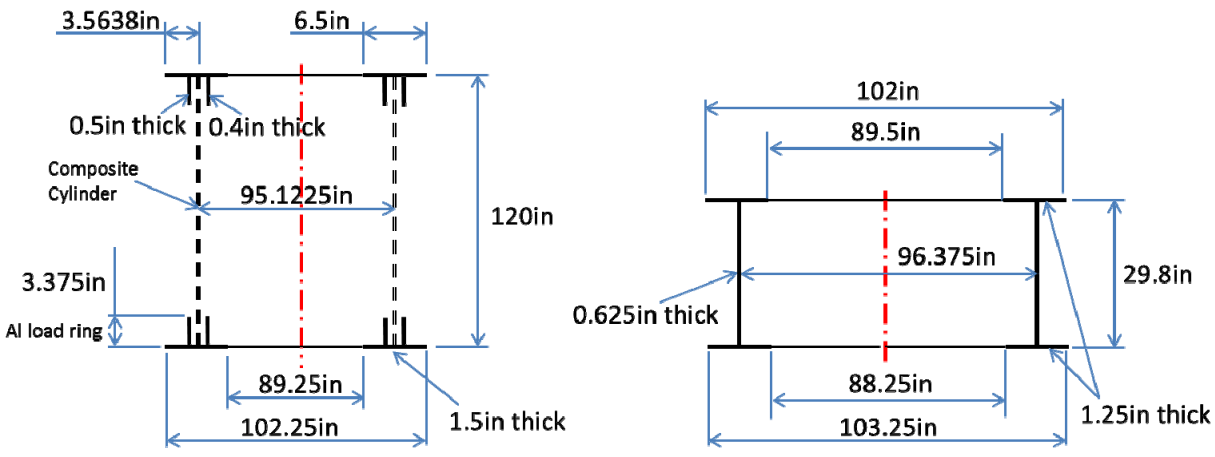

(a) Test article with aluminum end rings (b) Load-introduction cylinder

Figure 5. Geometry of (a) the test article with aluminum end rings, and (b) a load-introduction cylinder

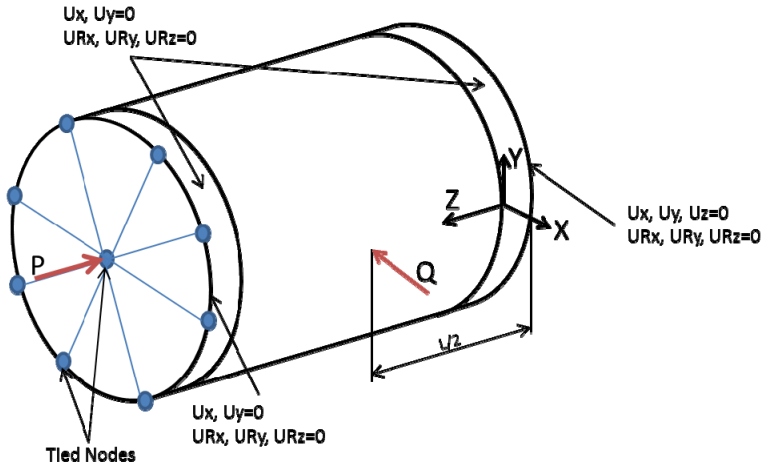

Figure 6. Sketch of the configuration 1 test article with boundary and loading conditions applied to 3.4-in. potted region of the test article.

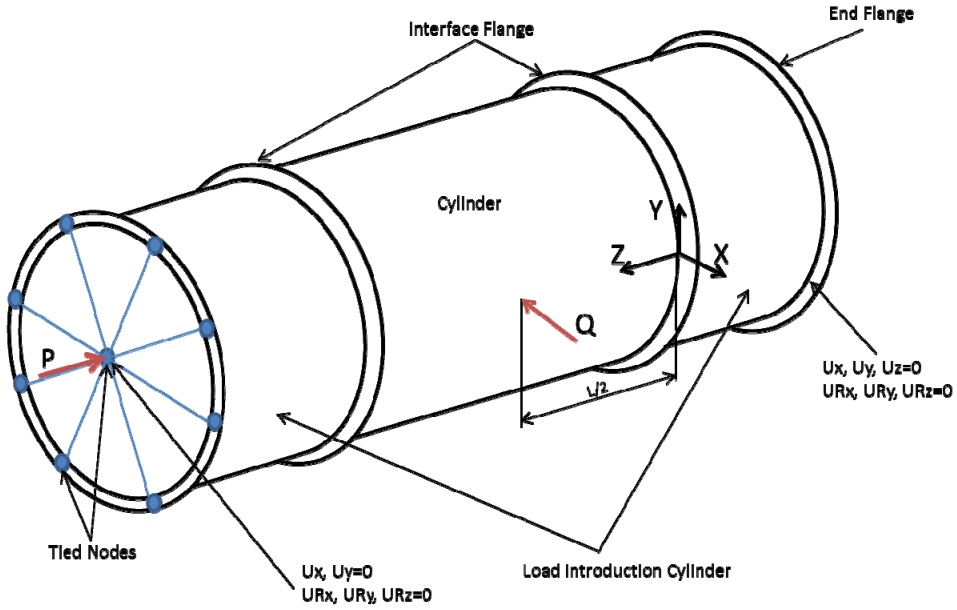

Figure 7. Sketch of the configuration 2 assembly with the test cylinder and load introduction rings.

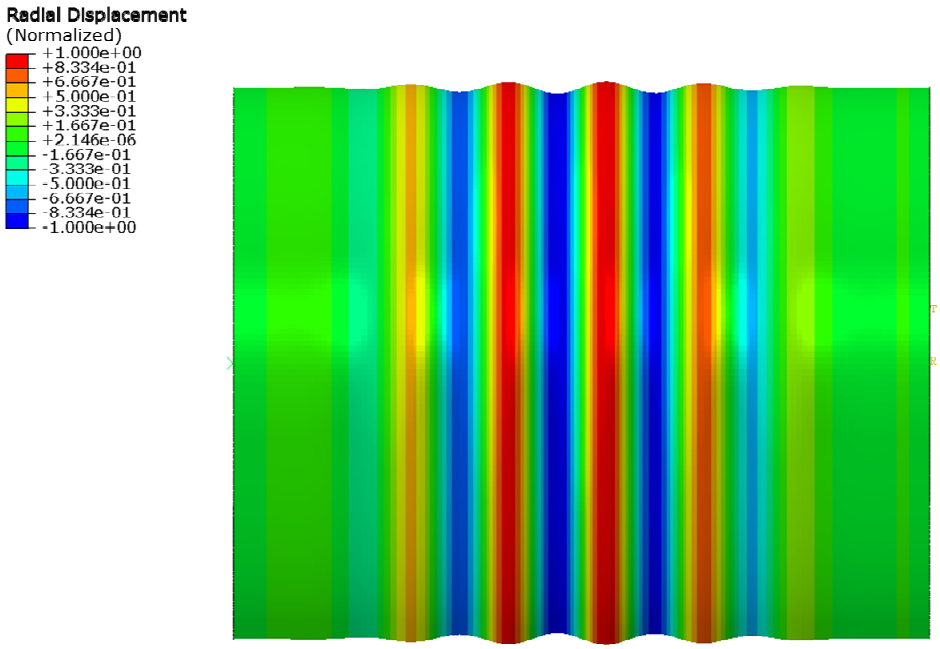

(a) Configuration 1

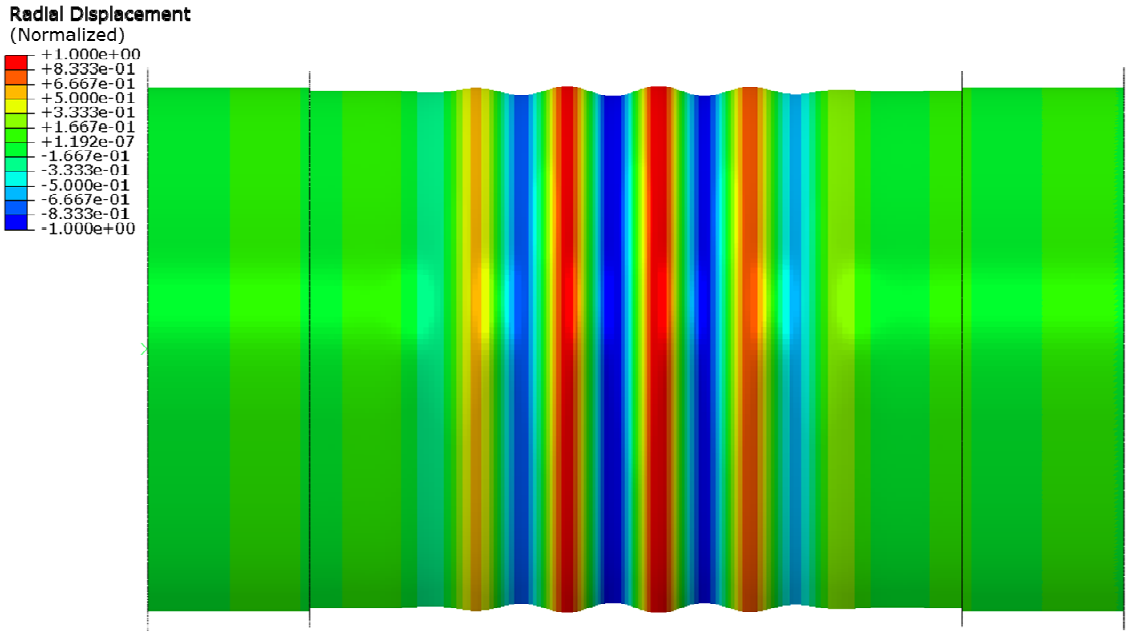

(b) Configuration 2

Figure 8. First predicted linear buckling eigenmode of (a) configuration 1, and (b) configuration 2.

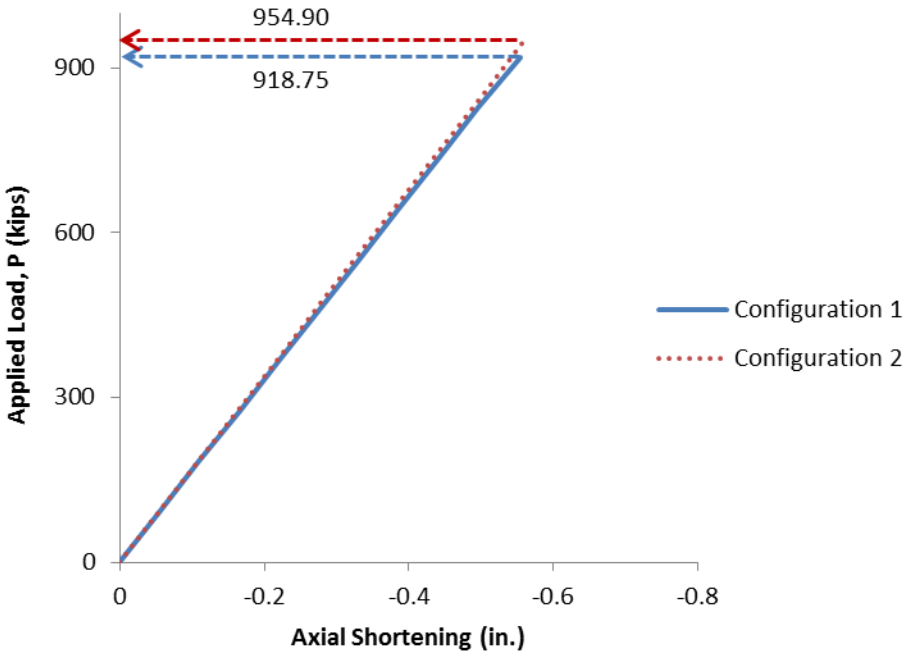

Figure 9. Applied load versus axial shortening from the nonlinear analyses.

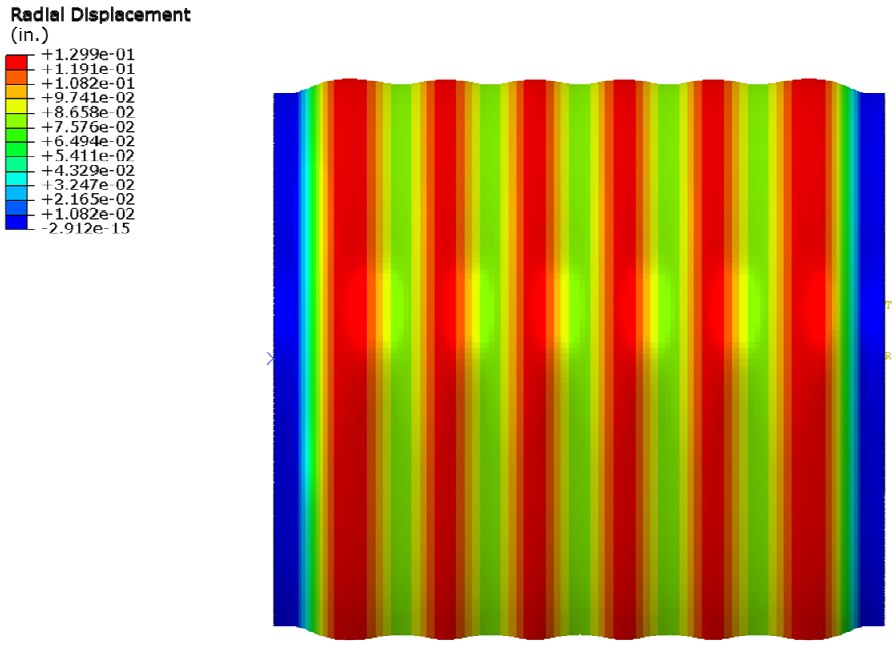

(a) Configuration 1

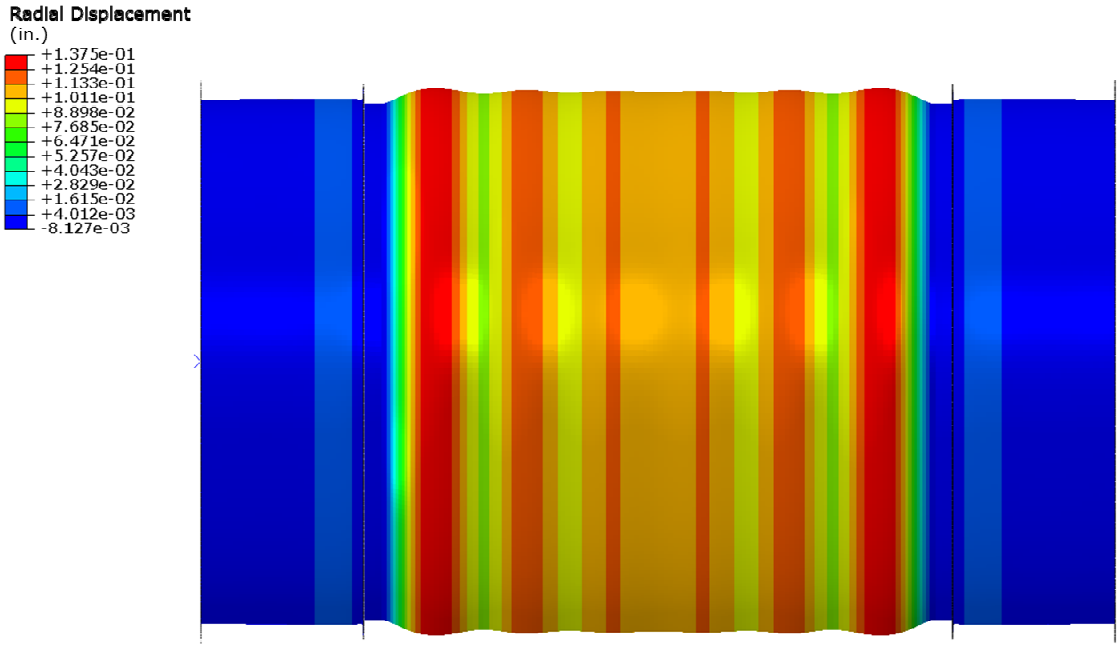

(b) Configuration 2

Figure 10. Predicted prebuckling radial displacements from the nolinear analyses at the P_{cr} of (a) configuration 1, and (b) configuration 2. Note the deformation scale factor is 20.

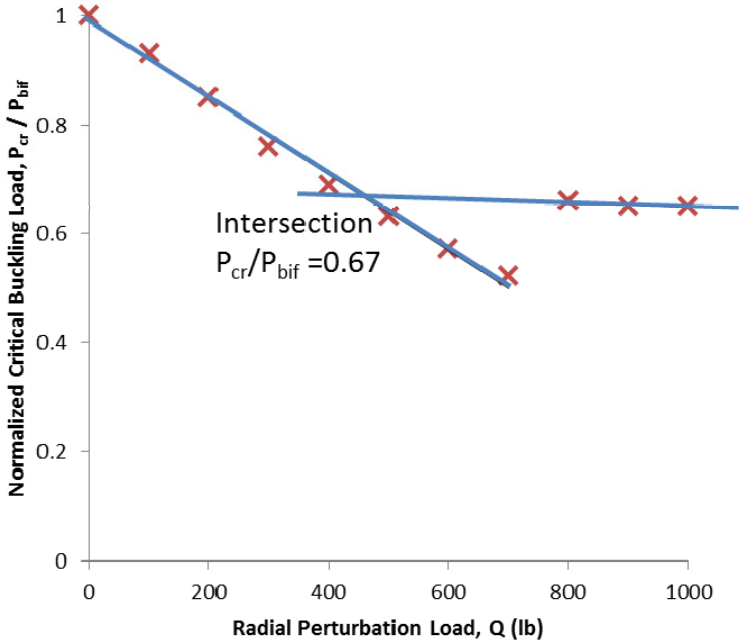

(a) Configuration 1

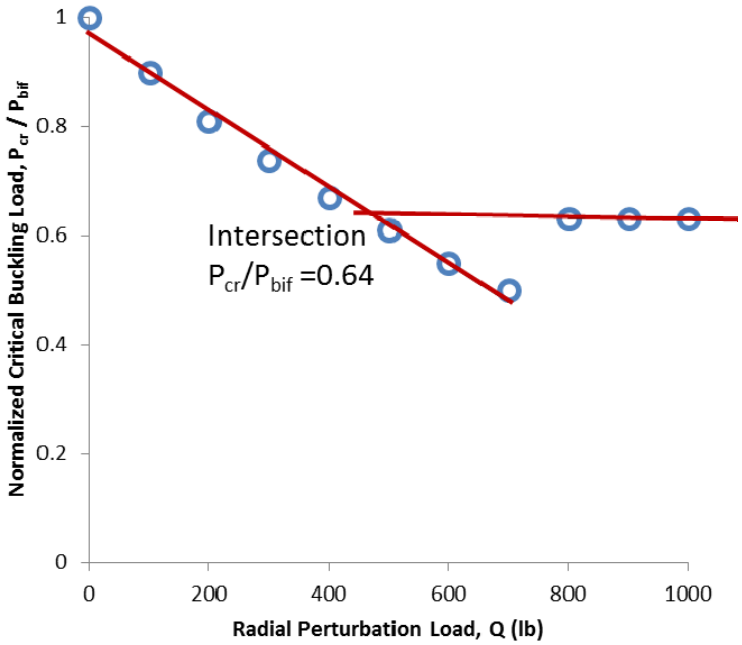

(b) Configuration 2

Figure 11. The normalized critical buckling load, P_{cr}/P_{bif}, plotted versus the radial perturbation load.

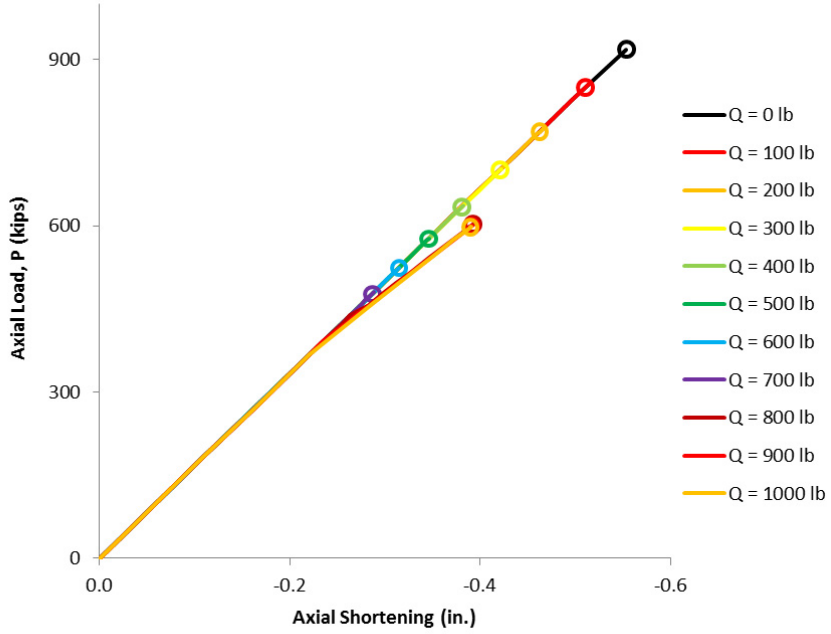

(a) Configuration 1

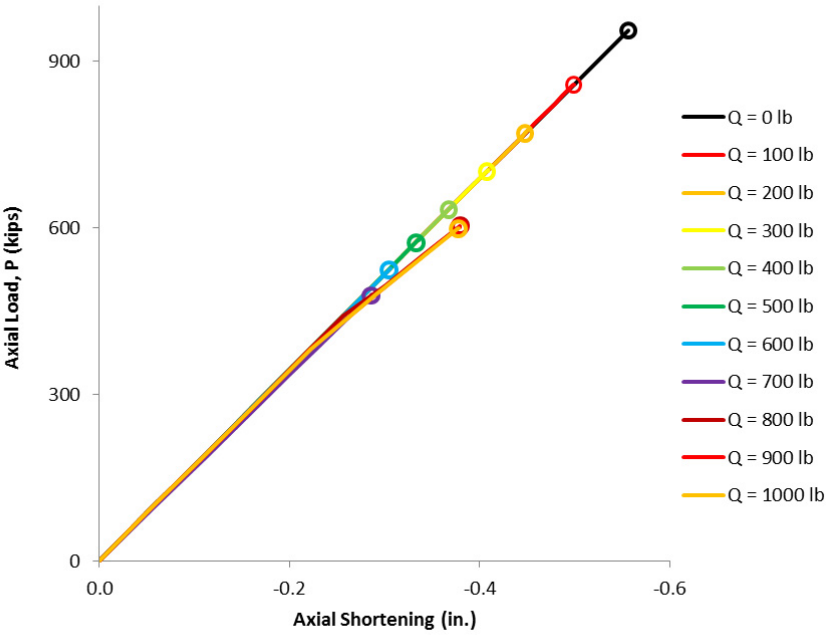

(b) Configuration 2

Figure 12. Axial load plotted versus axial shortening for several values of radial load.

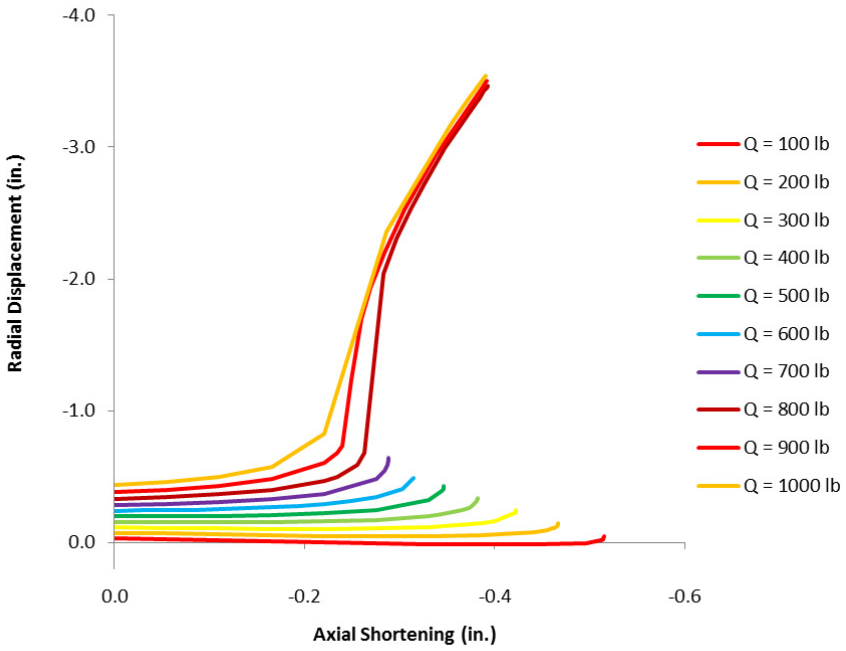

(a) Configuration 1

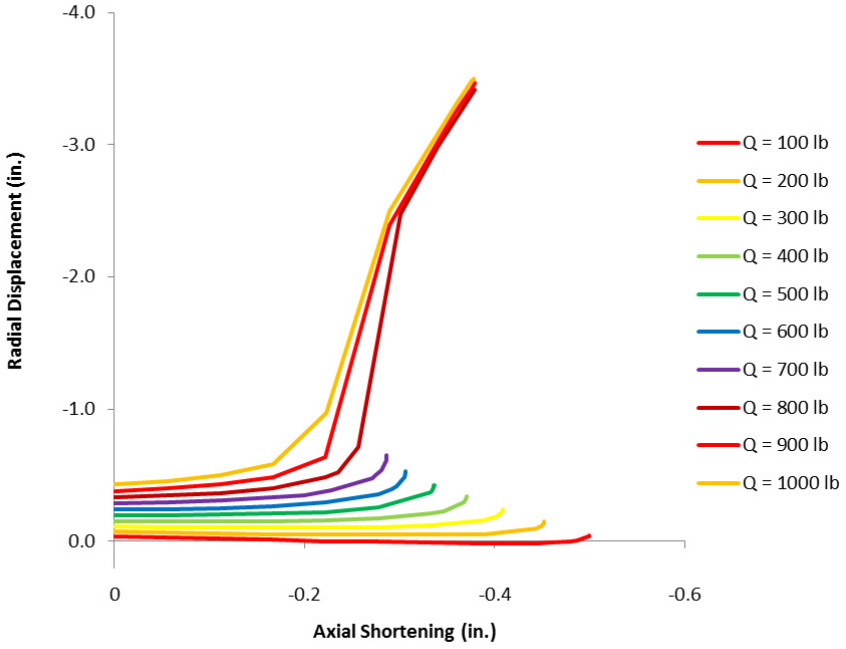

(b) Configuration 2

Figure 13. The radial-direction displacement at the point of application of the radial perturbation load plotted versus the axial shortening.

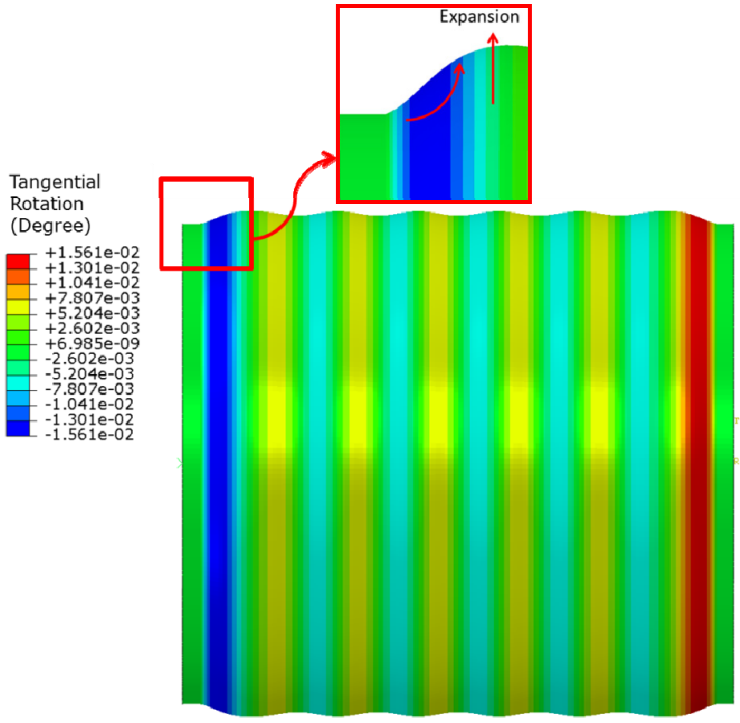

(a) Configuration 1

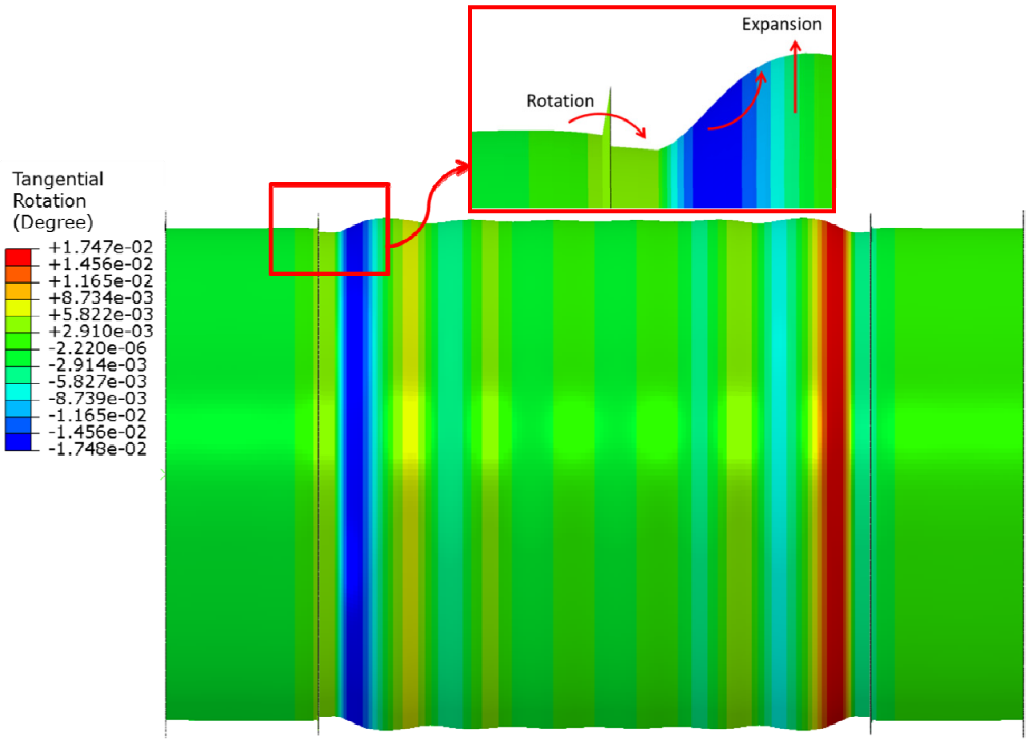

(b) Configuration 2

Figure 14. The tangential rotations for (a) configuration 1, and (b) configuration 2. Note the deformation scale factors are 20 for the main figures, and 40 for the inset figures.

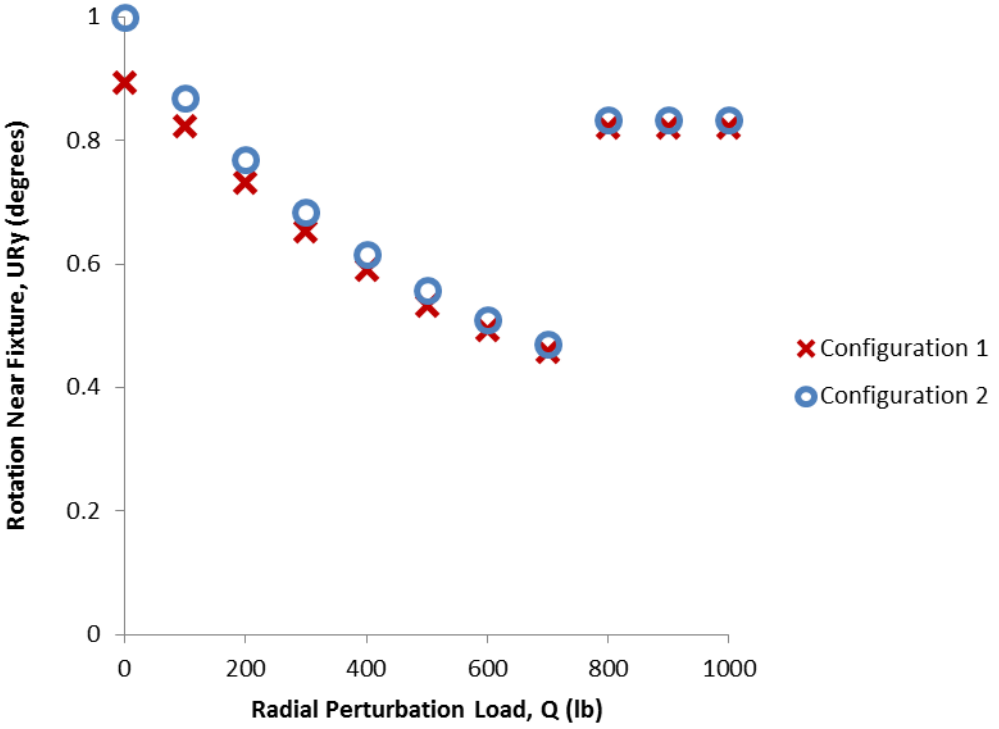

Figure 15. The tangential rotation near fixtures plotted versus the radial perturbation load.

Table 1. Assumed material properties and dimensions of IM7/MTM45 composite and honeycomb core structure.

IM7/MTM45	
E_1 (Msi)	20
E_2 (Msi)	1.25
ν_{12}	0.36
G_{12} (Msi)	0.77
G_{13} (Msi)	0.77
G_{23} (Msi)	0.385

Honeycomb Core	
E_1 (Msi)	0.00005
E_2 (Msi)	0.000038
E_3 (Msi)	0.06
ν_{12}	0.45
ν_{13}	0.0001
ν_{23}	0.0001
G_{12} (Msi)	0.0000175
G_{13} (Msi)	0.0295
G_{23} (Msi)	0.012

Al6061-T6	
E (Msi)	10.2
ν	0.33

A36 Steel	
E (Msi)	29
ν	0.26

Table 2. The first five linear buckling loads for configurations 1 and 2.

	Buckling Load (lb)				
Eigenmode	1	2	3	4	5
Configuration 1	924,190	924,740	924,740	924,820	926,040
Configuration 2	924,020	924,640	924,900	924,900	925,540

Table 3. Effective engineering properties of the facesheets.

E_y (Msi)	E_z (Msi)	G_{yz} (Msi)	ν_{yz}	ν_{zy}
5.97	8.31	3.26	0.308	0.429

REPORT DOCUMENTATION PAGE

Form Approved
OMB No. 0704-0188

1. REPORT DATE *(DD-MM-YYYY)*	2. REPORT TYPE	3. DATES COVERED *(From - To)*
01- 02 - 2013	Technical Memorandum	

4. TITLE AND SUBTITLE

Buckling Analysis of a Honeycomb-Core Composite Cylinder with Initial Geometric Imperfections

5a. CONTRACT NUMBER

5b. GRANT NUMBER

5c. PROGRAM ELEMENT NUMBER

6. AUTHOR(S)

Cha, Gene; Schultz, Marc R.

5d. PROJECT NUMBER

5e. TASK NUMBER

5f. WORK UNIT NUMBER

585777.02.40.04.03.50.07

7. PERFORMING ORGANIZATION NAME(S) AND ADDRESS(ES)

NASA Langley Research Center
Hampton, VA 23681-2199

8. PERFORMING ORGANIZATION REPORT NUMBER

L-20231

9. SPONSORING/MONITORING AGENCY NAME(S) AND ADDRESS(ES)

National Aeronautics and Space Administration
Washington, DC 20546-0001

10. SPONSOR/MONITOR'S ACRONYM(S)

NASA

11. SPONSOR/MONITOR'S REPORT NUMBER(S)

NASA/TM-2013-217967

12. DISTRIBUTION/AVAILABILITY STATEMENT

Unclassified - Unlimited
Subject Category 39
Availability: NASA CASI (443) 757-5802

13. SUPPLEMENTARY NOTES

14. ABSTRACT

Thin-walled cylindrical shell structures often have buckling as the critical failure mode, and the buckling of such structures can be very sensitive to small geometric imperfections. The buckling analyses of an 8-ft-diameter, 10-ft-long honeycomb-core composite cylinder loaded in pure axial compression is discussed in this document. Two loading configurations are considered–configuration 1 uses simple end conditions, and configuration 2 includes additional structure that may more closely approximate experimental loading conditions. Linear eigenvalue buckling analyses and nonlinear analyses with and without initial geometric imperfections were performed on both configurations. The initial imperfections were introduced in the shell by applying a radial load at the midlength of the cylinder to form a single inward dimple. The critical bifurcation buckling loads are predicted to be 924,190 lb and 924,020 lb for configurations 1 and 2, respectively. Nonlinear critical buckling loads of 918,750 lb and 954,900 lb were predicted for geometrically perfect configurations 1 and 2, respectively. Lower-bound critical buckling loads for configurations 1 and 2 with radial perturbations were found to be 33% and 36% lower, respectively, than the unperturbed critical loads. The inclusion of the load introduction cylinders in configuration 2 increased the maximum bending-boundary-layer rotation up to 11%.

15. SUBJECT TERMS

Honeycomb-core composite cylinder; Imperfection sensitivity; Radial perturbation; Shell Buckling

16. SECURITY CLASSIFICATION OF:			17. LIMITATION OF ABSTRACT	18. NUMBER OF PAGES	19a. NAME OF RESPONSIBLE PERSON
a. REPORT	b. ABSTRACT	c. THIS PAGE			STI Help Desk (email: help@sti.nasa.gov)
					19b. TELEPHONE NUMBER *(Include area code)*
U	U	U	UU	27	(443) 757-5802